Machine learning prediction of the mass and the velocity of controlled single-block rockfalls from the seismic waves they generate

Clément Hibert[1], Francois Noël[2,3], David Toe[5], Miloud Talib[1], Mathilde Desrues[1], Emmanuel Wyser[2], Ombeline Brenguier[6], Franck Bourrier[4], Renaud Toussaint[1,7], Jean-Philippe Malet[1], and Michel Jaboyedoff[2]

[1]Institut Terre et Environnement de Strasbourg / ITES, CNRS & University of Strasbourg F-67084 Strasbourg, France
[2]Institut des Sciences de la Terre / ISTE, University of Lausanne, Géopolis, CH-1015 Lausanne, Switzerland
[3]Geological Survey of Norway, NO-7491 Trondheim, Norway
[4]Université Grenoble Alpes, INRAE, ETNA, 38000 Grenoble, France
[5]Université Grenoble Alpes, INRAE, LESSEM, 38000 Grenoble, France
[6]Société Alpine de Géotechnique / SAGE, FR-38160 Gières, France
[7]SFF Porelab, The Njord Centre, Department of Physics, University of Oslo, P. O. Box 1048, Blindern, N-0316 Oslo, Norway

Correspondence: Clément HIBERT (hibert@unistra.fr)

Abstract. Understanding the dynamics of slope instabilities is critical to mitigate the associated hazards but their direct observation is often difficult due to their remote locations and their spontaneous nature. Seismology allows us to get unique information on these events, including on their dynamics. However, the link between the properties of these events (mass and kinematics) and the seismic signals generated are still poorly understood. We conducted a controlled rockfall experiment in the Riou-Bourdoux torrent (south French Alps) to try to better decipher those links. We deployed a dense seismic network and inferred the dynamics of the block from the reconstruction of the 3D trajectory from terrestrial and airborne high-resolution stereo-photogrammetry. We propose a new approach based on machine learning to predict the mass and the velocity of each block. Our results show that we can predict those quantities with average errors of approximately 10% for the velocity and 25% for the mass. These accuracies are as good as or better than those obtained by other approaches, but our approach has the advantage that it does not require the source to be localized, nor does it require a high-resolution velocity model or a strong assumption on the seismic wave attenuation model. Finally, the machine learning approach allows us to explore more widely the correlations between the features of the seismic signal generated by the rockfalls and their physical properties, and might eventually lead to better constraints on the physical models in the future.

1 Introduction

Slope instabilities are complex natural phenomena that pose a threat to humans and infrastructures in many regions of the world. Landslides, rockfalls, rock avalanches and surface collapses generating pit craters are natural disasters that can affect our societies. They also play a major role in the Earth surface dynamics as important erosion processes, whose occurrence might be caused by external factors such as earthquakes, intense precipitation or the thawing of ice in the joints and fractures

of large rocky masses for example. Understanding the triggering mechanisms, their dynamics, quantifying and documenting their properties and their spatio-temporal occurrences is of paramount importance to mitigate the associated risks but also to understand their contributions to long and short-term erosion processes. However, because of their spontaneous and destructive nature, gravitational instabilities are difficult to study.

Over the past two decades, these processes have been increasingly studied through the use of approaches based on seismology. Seismology makes it possible to augment the source of information conventionally deployed to study mass wasting processes (e.g. direct testimony, remote sensing, geomorphology, geodetic measurements, etc.) by its ability to provide information on event properties such as its exact time of occurrence (to the seconds) and its localisation (e.g., Norris, 1994; Deparis et al., 2008; Yamada et al., 2012; Hibert et al., 2014a; Dammeier et al., 2011, 2016; Gracchi et al., 2017; Dietze et al., 2017; Allstadt et al., 2018; Yan et al., 2019; Kuehnert et al., 2020b), with the possibility of recording them over vast distances (up to 1000 kilometers for the largest events) (e.g., Kanamori and Given, 1982; Kanamori et al., 1984; Ekström and Stark, 2013; Allstadt, 2013; Hibert et al., 2019). More than providing spatio-temporal information, sometimes in real-time, seismology offers the possibility to retrieve the dynamics of an event through the information carried by the seismic signal emitted during the triggering and the propagation of the event. There are very few other observational approaches that allow retrieval of important insights on the dynamics. Hence finding relationships between seismic signals generated by gravitational instabilities and their properties has been a major focus of recent research in landslide and rockfall seismology.

For catastrophic landslides (volume over 1 million cubic meter), approaches based on the inversion of the long-period (low-frequency, below 0.5 Hz) seismic waves have been proposed. By retrieving the force exerted by the mass displacement on the Earth those approaches have successfully helped to determine dynamic parameters (velocity, momentum, acceleration) and properties of these events (e.g., Kawakatsu, 1989; Ekström and Stark, 2013; Allstadt, 2013; Zhao et al., 2012; Iverson et al., 2015; Hibert et al., 2014b, 2017a; Moore et al., 2017; Dufresne et al., 2019; Li et al., 2017; Moretti et al., 2020; Chao et al., 2018; Zhang et al., 2019). However most of mass wasting processes that occur worldwide do not have a volume large enough to generate those long-period waves, thus precluding the use of inversion methods to retrieve their dynamics quantities. Yet, those mass wasting processes will generate high-frequency seismic waves (frequency above 1 Hz). Being able to infer physical properties from those high-frequency seismic waves will therefore allow us to characterize most mass wasting processes, including smaller-volume events, which is critical to have a better understanding of the occurrence and the physics of those phenomena and thus for mitigating the risks they generate.

Recent studies proposed scaling laws between high-frequency seismic signal features and source properties of rockfalls and landslides. These studies are mostly based on laboratory experiments (e.g., Farin et al., 2015, 2016, 2019; Arran et al., 2020), real-scale experiments (e.g., Bottelin et al., 2014; Hibert et al., 2017b; Saló et al., 2018), and documented natural events (e.g., Norris, 1994; Deparis et al., 2008; Dammeier et al., 2011; Hibert et al., 2011; Levy et al., 2015; Hibert et al., 2017a; Le Roy et al., 2019). Among the quantities studied, several correlations between the mass and the velocity of the rockfall, and the magnitude, the maximum amplitude at the source and the seismic energy of the seismic signal have been observed and sometimes quantified. Several scaling laws have been proposed (e.g., Norris, 1994; Deparis et al., 2008; Hibert et al., 2011; Levy et al., 2015; Hibert et al., 2017b; Saló et al., 2018; Le Roy et al., 2019) but are all carrying strong uncertainties, caused mainly by

the simplicity of the propagation models used (e.g., Le Roy et al., 2019; Kuehnert et al., 2020a), the difference of contexts (soft soil vs. hard rock, influence of the seismic network geometry) and the physics of the source (free-fall, granular flows, single rockfall, multiple rockfalls). However all those studies demonstrated that there is a link between some seismic signals features (maximum amplitude at the source, seismic energy, local magnitude) and some source properties (mass, velocity, energies, momentum, force or acceleration). The difficulty resides now in understanding the fundamental physics that explains those correlations, as well as in increasing the accuracy of the scaling laws proposed. This is deemed important as it opens the perspective to quantify mass movement dynamics directly from the seismic signals they generate (i.e. without inversion or modelling). This is critical for the development of future methods aimed at their real-time detection and characterization using high-frequency seismic signals. This can be achieved by improving both the source physical model and seismic waves propagation model which remains a strong challenge for high-frequency seismic waves. These improvements require more high-quality observations to calibrate and validate the models. This is what motivated the 2018 Riou-Bourdoux controlled rockfall experiment, which followed and improved upon a similar experiment conducted in 2015 (Hibert et al., 2017b).

Thanks to the deployment of a dense seismological network close to the block impacts, and an approach allowing an accurate reconstruction of the trajectories (Noël et al., 2022), we tried to complete three objectives: 1) Better understand and model the propagation of the seismic waves generated by the block impacts; 2) Find and try to better constrain the correlations between the kinematic parameters of the impacts of the blocks and the features of their seismic signals; 3) Explore the use of an innovative approach based on a machine learning algorithm to infer the mass and the velocity of the block at each impact from the seismic signals they generate.

2 Material and methods

2.1 Context : the Riou-Bourdoux catchment

The Riou-Bourdoux is a torrential catchment located in the South French Alps, approximately 4 km north of the city of Barcelonnette (France). It formed in callovo-oxfordian black marls whose high erosion susceptibility resulted in the formation of numerous steep ($>$ 30 degrees) gullies. The blocks were launched in a gully located on the north slope of the torrent. The travel path had a length of approximately 200 m and slope angles ranging from 45 degrees on the upper part of the slope to approximately 20 degrees on the terminal debris cone (Figure 1). The launched elements consisted in hard limestone blocks selected in the torrent and brought to the launch pad with a backhoe.

2.2 Block trajectories and properties measurements

Kinematic parameters of each launch were computed from 31 reconstructed rockfall trajectories using the ballistic equations of a free-falling object neglecting the drag from the air (Volkwein et al., 2011; Wyllie, 2014; Loew et al., 2021). The back calculation method using 3D terrain models and video footage (Noël et al., 2017; Noël et al., 2022) requires accurately measuring

the geometric features of each launched block and of the terrain, and to track their propagation with high speed multispectral cameras from different view angles.

31 limestone blocks were individually weighted using a lift and a tension load cell. The density of the rocks were determined in the laboratory from analysis conducted on core samples taken from each block. The block shapes were acquired using mobile handheld terrestrial laser scans (mobile terrestrial laser scanning / GeoSLAM ZEB-Revo) and from Structure-from-Motion photogrammetry (SfM) using pictures acquired with a Panasonic GH5 camera and the software Agisoft Metashape Pro v.1.4.4. The LiDAR model has a spatial density of about 50,000 points per m^2 at the block level. The SfM model was build from 128 photos for each block and has a density of about 5 millions points per m^2 when scaled (average: 4.9310^6 pts/m^2; standard deviation: 2.12310^6 pts/m^2). Assuming a homogeneous distribution of the mass, the moments of inertia of each block and the main axes of inertia were identified from the 3D models of each block and the density. Their dimensions were measured on the 3D models aligned on their main axes of inertia. The masses of the blocks ranged from 39 to 468 kg.

A very-high resolution terrain model of the gully (Figure 1) was acquired using four acquisition methods to ensure proper coverage of occluded faces, detailed texture of the surfaces and accurate scale and orientation relative to the horizontal. A highly detailed terrain SfM model was generated from georeferenced pictures acquired with a DJI Phantom 4 UAV flying at an average altitude of 25.3m. We use the software Agisoft Metashape Pro v.1.4.4. The model was built from 167 photos, with resolution of 5472×3078 pixels, and with a selected overlap of at least 9 images. The initial model had 345922467 points, with a ground resolution of 6.32mm/pix, and was downscale to 83475710 points spaced by 1 cm. Its scale was then adjusted by less than 1% using the iterative closest point algorithm to match with a detailed terrain model obtained from four locations with a terrestrial laser scanning device (Optech ILRIS-LR). The main gully was also scanned with a mobile terrestrial laser scanning while rappelling down, to cover every part in detail. Finally, evenly spread targets were painted in the upper and lower part of the gully and were located using a laser theodolite.

The blocks were pushed down manually one by one separated by about 5 to 10 minutes. Their trajectories were manually tracked from up to 8 viewpoints: five viewpoints had fixed framing, being installed on tripods (one in the middle part of the travel path and four at the bottom of the gully); two viewpoints were from the sky using two DJI drones, one flying in hover and one following the motion of the blocks; the last viewpoint was from a camera panned manually to track the rocks using a long-focus lens and was located at the bottom of the gully. An exhaustive description of the experiment, the approach to reconstructing the trajectories, as well as videos showing the propagation of the blocks and the numerical approach to reconstructing the trajectories is given in the paper by Noël et al. (2022), companion to the present article.

2.3 Seismic network and data

The seismic network was deployed along the gully. The network comprised 16 3-components geophones (4.5Hz/3C connected to a Daqlink seismic camera at a sampling rate of 1000 Hz). The exact position of the sensors were measured by differential GNSS (Figure 1). In this analysis, we used only the vertical components of the geophones as we observed the best signal-to-noise ratio on this component. Data from the geophones number 14 and 16 were discarded as the records exhibited high

amplitude noises and spikes probably related to a faulty connection or a bad installation. Before analysis each record was deconvolved from the instrument response to get the ground velocity. No filtering was applied to the raw data.

2.4 Trajectory and kinematics reconstruction

The impact locations of each block were pointed on the 3D textured detailed terrain model (Figure 1). The task was eased by using a custom developed software (Noël et al., 2022) in which the terrain can be visualised from the same viewpoints as the corresponding video footage, and in which the reconstructed trajectories offset by the radius of each rock are updated in real-time following the cursor mouse or manually entered impact coordinates. The position and time of each impact can thus be accurately defined until obtaining visually matching trajectories with those visible in the camera footage. With non-optimal viewing angles or terrain texture with little contrast, screenshots of the terrain model and video footage were aligned with the Handle Transform Tool in the GIMP software using the surrounding elements of texture in order to find the exact location of the impact.

The trajectories were exported with their velocities and vectors normal to the terrain and the center of mass of the blocks is extrapolated from the impact position on the ground. All trajectories were further visually inspected in the CloudCompare software. The angular velocities were obtained by averaging the number of block revolutions performed during the period in between each impact. The average axis around which the block rotated was identified to estimate the angular momentum based on the geometric features of each block.

In total, 376 impacts were available from 25 trajectory segments composed of many parabolas. The impacts at the extremities of each segment are missing because of missing incoming/outcoming velocities. Therefore, 326 impacts were reconstructed with their incoming and outgoing translational and angular velocities, kinetic energy changes and momentum.

2.5 Trajectories and seismic records synchronization

While the seismological data could be time-stamped by a GNSS, the clocks of the different cameras used during the experiment are not all set to the absolute time. To determine the lag between the two times series (time of impact from the direct observations and seismic records) with a precision below the second, we performed a cross-correlation analysis. The timing of the impacts was transformed into a time series of zeros and ones, zeros indicating the times with no impact and ones the time of each impact. We then normalized the seismic records by the maximum of the envelope and computed the cross-correlation between the impacts time series and the normalized envelope of the seismic records, with lags ranging from minus 10 seconds to plus 10 seconds. The lag for which the best normalized correlation was observed was selected. A manual control and final adjustment of the results has been performed. After this first step we manually picked the beginning and the end of each seismic signal on each station. We selected only the signals associated with impacts that did not result in the fracturing of the blocks and that were not generated by parts of fragmented blocks. This was verified for each impact on the videos of the launches. We also selected only impacts for which it was possible to pick clearly the beginning and the end of the seismic signal and therefore discarded all intricate and low amplitude seismic signals. An example of the seismic signals recorded at one station and of the selected impact seismic signals is presented in Figure 2. This resulted in a dataset of 384 seismic signals of impacts.

2.6 Seismic sources parameters computation

There are essentially two properties of the high-frequency seismic signals generated by mass movements that have been studied in correlation with the physical parameters of the source dynamics, the maximum amplitude of the seismic signal corrected for propagation effects A_0, and the energy of the seismic signal at the source E_s (e.g., Norris, 1994; Deparis et al., 2008; Dammeier et al., 2011; Schneider et al., 2011; Hibert et al., 2011; Bottelin et al., 2014; Levy et al., 2015; Farin et al., 2015, 2016; Hibert et al., 2017b, a; Saló et al., 2018; Le Roy et al., 2019; Farin et al., 2019; Arran et al., 2020). These two quantities are usually compared to the source velocity, momentum, and its kinetic and potential energies. Both quantities are computed from attenuation parameters that allow to account for the attenuation of seismic waves caused by the propagation of waves in the Earth and which are caused by geometrical spreading and anelastic attenuation. Determining an adequate attenuation model is therefore critical.

Thanks to the reconstruction of the trajectories, in our study we know the exact location of the impact and hence the exact distances between the source and the receivers, thus we could test several attenuation models and find the one that better explains the observed decay of the amplitudes with the distance. The best model should be the one that allows the best regression of the maximum amplitude of each impact recorded at each station as a function of the distance of those stations to the location of the impact.

We tested three simple attenuation models, one for surface wave (Eq. 1) and one for body wave (2), both proposed by Aki and Chouet (1975), which consider the anelastic attenuation of seismic waves through the use of the attenuation factor β :

$$A(r) = A_0 \frac{e^{-\beta r}}{\sqrt{r}}, \tag{1}$$

$$A(r) = A_0 \frac{e^{-\beta r}}{r}, \tag{2}$$

The maximum amplitude at the source A_0 and the β factor can be determined directly from the attenuation model for each impact.

An approximation of the seismic energy for body-waves can be computed as Crampin (1965):

$$E_s = \int_{t_i}^{t_f} 4\pi r^2 \rho c u_{env}(t)^2 e^{\beta r} dt, \tag{3}$$

with :

$$u_{env}(t) = \sqrt{u(t)^2 + Ht(u(t))^2}, \tag{4}$$

where Ht is the Hilbert transform of the seismic signal $u(t)$ used to compute the envelope $u_{env}(t)$, t_i and t_f the times of the beginning and the end of the seismic signal respectively and ρ the density of the layer through which the generated surface

waves propagate, and c their phase velocity. The average velocity of body waves in black marls is approximately 450 $\mathrm{m.s^{-1}}$ (Hibert et al., 2012; Gance et al., 2012). The density ρ of dry black marls is approximately 1450 $\mathrm{kg\,m^{-3}}$ (Maquaire et al., 2003). For each impact we computed the seismic energy at each station and kept the mean over all stations.

2.7 Machine Learning: using Random Forests as a regression tool

Random Forests (Breiman, 2001) is a machine learning algorithm based on the computation of a large number of decision trees. Decision trees are top-down structures consisting of nodes and branches. At each node a statistical test is performed on the value of one feature of the input data. The outcome of this test tells which branch to use to get the next node. The final nodes of the tree give the decision of the tree. The randomness comes from the use of a random subset of events from the dataset and of features used to characterize the events to build each tree. Each decision tree in the "forest" is therefore different and the model combines hundreds (if not thousands) of decision trees.

Random Forests is now successfully used in seismology for automated source classification (Provost et al., 2017; Hibert et al., 2017c; Maggi et al., 2017; Malfante et al., 2018; Hibert et al., 2019; Ao et al., 2019; Pérez et al., 2020; Wenner et al., 2021; Chmiel et al., 2021). However the Random Forests algorithm can also be used to estimate continuous values and thus perform regression analyses. The model will then not give a class (e.g. an integer) but an estimation of a value that exists in a continuum. A Random Forests classifier is able to identify the origin of a seismic source (for example landslides, earthquakes, mining blasts, etc.) while a Random Forests regressor is able to predict (in a statistical machine learning sense) the time of occurrence of laboratory-triggered earthquakes (e.g., Rouet-Leduc et al., 2017). For a classification application of the Random Forests algorithm the predicted class is given by the majority vote of all the trees. For a regression, the mean of the predicted values by each tree is the final result.

In this study we exploit Random Forests as a regression tool to "predict" the mass and the velocity of the rockfalls from the features of the seismic signal generated by each impact at the ground. The methodology consisted in: 1) defining relevant seismological features to characterize the data; 2) defining a subset of the dataset to train the Random Forests model; 3) training the model and 4) testing the model on a subset of the dataset (the test set) not selected for the training. To assess the robustness and estimate uncertainties associated, steps 2 to 4 are repeated hundreds of times, by increasing, from 10 to 100, the number of events in the training set.

When selecting seismic signals features we must find those that might carry the most relevant information on the source properties. We choose 57 features proposed by Provost et al. (2017) and Hibert et al. (2017c) and given in Appendix A. Those features are used for many applications of the Random Forests as an automated seismic source classifier. They can be categorized into three families: 1) waveform features (temporal); 2) spectral (frequency) features and 3) pseudo-spectrogram (evolution of the frequency content with time) features. When analysing a dataset from multiple stations, it might be complicated to merge the information carried by all signals in the same set of features. To extract information about the mass and velocity of the source, we computed each feature value for a given impact at each station and took the mean value across all stations. We also calculated the standard deviation of each feature value across all stations, as we believe that information about mass and velocity may be present in the differences or, conversely, in the closeness of the observed values of the features. These

standard deviations are included in our feature table. Therefore, we have a total of 114 features for each impact, comprising 57 mean values and 57 standard deviation values. Each impact seismic signal is considered as a sample in our dataset. As for the A_0 and E_S computation, we considered only the impact for which the attenuation regression model yields a determination coefficient above 0.6. The maximum amplitude at the source A_0 and the seismic energy E_S are not included in the features used.

By analysing the machine learning model produced we can determine which features of the seismic signals carry the important information that the model is using to successfully predict the value of the mass and the velocity of the block at each impact. This might provide insights on the link between the dynamics of the block and the seismic source. This is possible by computing the importance score of each feature, which accounts for the relative contribution of each feature in the success of the regression. The value of the importance of each feature is computed by permuting the values of a given feature in the features array, and assessing how this permutation impacts the regression results. If the permutation of a given feature value results in a worse overall fitting of the real values than the predicted ones, then the feature is important in the regression process. Conversely, if the prediction accuracy remains the same while permuting a feature value, then this feature has little impact in the regression process. The importance is given by a normalized score. The higher is the score of the feature the higher is its importance in the prediction process.

In this work we set the number of decision trees in the forest to 1000. We choose a split criterion based on the Gini index. We set the number of predictors (features) considered for each split as the square root of the total number of features. We trained and tested the machine learning model with an increasing number of samples, from 10 to 100 with a step of 10. For each case (10 to 100 samples), we repeated the process of training and testing the algorithm 100 times, to assess the robustness of the model.

3 Results

3.1 Attenuation models

Figure 3 shows the maximum amplitude recorded at each station for each impact of the launch of Block #1. The maximum amplitude of the signal is decreasing with the distance r of the sensor to the location of the impact as expected. For each attenuation model we computed the regression line and assess the quality of the regression by computing the determination coefficient R^2. This was performed for each selected impact. The mean of the R^2 coefficient for the body wave model and the surface wave model are, 0.70, and 0.64 respectively. For 363 over a total of 384 impacts, the best regression model between the maximum amplitude and the distance between the impact and the sensors is the model 2, which assumes body-waves propagation. Therefore for the computation of A_0 and E_S we choose to use the body wave model. For the analysis of the correlation and the test of the machine learning approach we selected the 298 impacts for which the attenuation model was able to fit the real data with a coefficient R^2 of at least 0.6. All the other impacts were excluded to avoid including too peculiar events. Low R^2 values might be explained by irregular kinematic behaviours such as the block hitting an obstacle (trees, other

rocks), multi-impacts in a very short time, composite contacts or sliding of the block, or an impact being too far from the seismic network.

3.2 Correlations between the seismic and trajectography parameters

For 298 impacts we analyse the relationship between two seismic quantities (A_0 and E_S) and nine kinematic parameters : the incident northbound, eastbound and vertical velocity and the incident velocity modulus (Vix, Viy, Viz and $|Vi|$), the incident and the rebound momentum (Pi and Pf), the incident and rebound kinetic energy (Ei and Ef) and the difference between those two energies ($Ef - Ei$). The X-axis is oriented east to west and the Y-axis is oriented south to north. For each pair, we tested simple linear regressions and computed determination coefficients (Figure 4).

The best correlations are observed between the incident velocity modulus $|Vi|$ and the maximum amplitude at the source A_0, and between the incident kinetic energy E_i and the seismic energy E_s, with determination coefficient R^2 of 0.43 and 0.39 respectively. The worst correlation is observed between the northbound velocity and A_0 with a R^2 of 0.04.

3.3 Mass and velocity predictions

We assessed the quality of the predicted results by computing the difference in percent between the predicted and the measured values of the blocks mass and of the modulus of the velocity inferred from the kinematic reconstruction presented in Noël et al. (2022). Therefore a difference of 0% is reached when the predicted value is equal to the real value. In table 1 we present the median error of the prediction on the 100 instances of training-test the algorithm as a function of the number of samples used to train the model (10 to 100). The median values, which are less impacted by outlier values, are reported in Tab 1. The mean, the median and the complete distribution of the error on the prediction of the mass and the velocity for the cases of model training with 10 to 100 samples are presented on Figure 5.

Number of training samples	Average error on velocity [%]	Average error on mass [%]
10	19.0	43.3
20	16.3	39.0
30	15.2	36.6
40	13.9	34.6
50	13.4	32.9
60	12.7	31.1
70	12.1	29.8
80	11.6	28.6
90	11.2	26.6
100	10.7	25.3

Table 1. Predictions result: percentage of error between the real and the predicted values

As shown in Table 1 and Figure 5, with 10 samples used to train the model, we reach a median of the prediction error of 43.3% on the mass and 19.0% on the velocity. Those values drop to 32.9% and 13.4% for 50 samples, and to 25.3% and 10.7% for 100 samples. When training the model with 10 samples we underestimate the mass (the predicted mass is lower than the real mass) for 39.8% of the events and we underestimate the velocity for 49.0% of the events. When training the model with 50 samples we underestimate the mass for 37.6% of the events and we underestimate the velocity for 49.6% of the events, and when training with 100 samples we underestimate the mass for 38.0% of the events and we underestimate the velocity for 48.9% of the events.

3.4 Features importance

Figure 6 presents the mean importance scores of the features for models aiming at predicting the mass and the velocity and trained with 100 samples. For the mass prediction, the 20 best features are based on the waveforms (8 features) and the pseudo-spectrograms (11 features). Only one spectral feature appears in the top-20. The 5 most important features are the mean of the seismic energy in the 5-10 Hz frequency band (#13), the mean of the seismic energy in the 10-30 Hz frequency band (#14), the mean ratio between the envelope of the maximum frequency over the envelope of the mean frequency (#43), the mean ratio between the envelope of the second quartile of the frequency spectrum over the envelope of the first quartile of the frequency spectrum (#55), and the mean ratio between the envelope of the third quartile of the frequency spectrum over the envelope of the first quartile of the frequency spectrum (#57).

For the velocity prediction, the 20 best features are also mostly based on the waveforms (10 features) and the pseudo-spectrograms (7 features), with only three spectral features appearing in the top-20. The 5 most important features are the standard deviation of the seismic energy in the 100-200 Hz frequency band (#74), the mean of the seismic energy in the 100-200 Hz frequency band (#17), the standard deviation of the values of the energy of the seismic signal in the 50-100 Hz frequency band (#72), the standard deviation of the difference between the envelope of the maximum frequency over the envelope of the median frequency (#111) and the standard deviation of the values of the energy of the seismic signal in the 30-50 Hz frequency band (#71).

We can note that 1) none of the best 5 features are the same for the mass and the velocity prediction, 2) only 6 features are common in the top-20 for both quantities and 3) mass prediction uses none of the features computed from the standard deviation of the features computed at each station (features with numbers above #57) while the model for velocity prediction uses 4 of them in the top-5. Finally most of the top 5 features for the mass and the velocity prediction are based on a difference of energy in several frequency bands.

4 Discussion

4.1 Correlations between the seismic and trajectography parameters

Figure 4 shows qualitative correlations between the momentum, the kinetic energy, the maximum amplitude at the source and the seismic energy, as observed or modelled in previous studies (Deparis et al., 2008; Vilajosana et al., 2008; Hibert et al., 2011; Levy et al., 2015; Farin et al., 2015; Hibert et al., 2017b; Farin et al., 2016; Saló et al., 2018; Le Roy et al., 2019). Our results suggest that the kinetic energy before impact is better correlated to the seismic energy than the loss of kinetic energy between the impact and the rebound $Ef - Ei$. The block travel directions were mostly from West to East along the gully morphology. The lack of strong displacement in the North-South direction, and hence the low velocity values, might explain the poorest correlation observed between Viy and A_0.

However most R^2 values are low for all the correlations investigated. Those weak quantitative correlations precluded us from using the scaling laws to estimate the mass and the velocity of the blocks at each impact as proposed in (Hibert et al., 2017b) because it would result in very high uncertainties on the inferred masses and velocities. As demonstrated by (Kuehnert et al., 2020a), velocity-depth profile, 3-D soil heterogeneities, source direction and the topography play a major role in the modulation of the waveforms and the amplification of both the maximum amplitude and the energy of the generated seismic signals. Those effects are not taken into account in the simple attenuation models used in this study and numerous previous ones. We are starting to have access to complex models that can take into account some of these effects for high frequency seismic signals (Kuehnert et al., 2020a), but they require high computational time and a comprehensive knowledge of the context physical properties (velocity profile, 3-D medium heterogeneities, etc.), which can be difficult to get for real conditions. Having access to these models to perform direct modeling or inversion of the source parameters might be laborious and expensive to reproduce in different contexts, preventing an hypothetical easy portability of the approach for operational uses. This motivated the exploration of the machine learning approach to infer the properties of the rockfall without needing any attenuation model or an $apriori$ knowledge of the medium.

4.2 Seismic signal features importance and physical model

The force imparted by an elastic sphere on a solid elastic surface can be described by the Hertz contact theory (Hertz, 1882), as proposed by (Farin et al., 2015), and was demonstrated to be relevant to model the force created by a block impacting the ground in experimental and natural experiments (Farin et al., 2015; Bachelet et al., 2018; Kuehnert et al., 2020a). These studies have shown that, in the framework provided by the Hertz theory, the seismic signals maximum amplitude, energy, corner frequency or the variance of the spectra are controlled by the velocity, the mass, the duration of the impact and the physics and the geometry of the contact of a single block with the ground. Therefore the seismic signals maximum amplitude, energy, corner frequency or spectrum variance carry information on the dynamics and properties of the impacting block, and might be analysed to retrieve those physical quantities, and especially the force, the velocity and the mass of the impactor.

The Random Forest model we trained yields information on which features of the seismic signal carry the most important information to successfully predict the mass and the velocity. We observe that the most important features used to predict the

velocity are not exactly the same as those used to predict the mass. However the absolute seismic energy in several frequency bands (Features #13-17 and #70-74) is an important information for both the prediction of the mass and of the velocity. This is consistent with the works by (e.g., Huang et al., 2007; Farin et al., 2015; Hibert et al., 2017b; Kuehnert et al., 2020a), which have shown that the radiated seismic energy and the frequency content of a seismic signal generated by an individual impactor scales with its mass and velocity. Hence by including the energy of the seismic signal filtered in different frequency bands as features in our predictive model we can retrieve this correlation and allow the model to do accurate prediction.

We have observed a discrepancy in the importance of the features used for predicting mass and velocity in a specific set of features (#13-17 and #70-74). While the standard deviation of feature values has a significant impact on the prediction of velocity, it does not affect the prediction of mass. This suggests that differences in seismic energies recorded at different stations are crucial for predicting velocity, but not mass. Additionally, energy in lower frequency bands plays a significant role in predicting mass, while energy in the highest frequency band is important in predicting velocity, as indicated by features #37 and #94. Due to the attenuation of high-frequency seismic waves during propagation, seismic signals recorded at closer stations may be more important in determining velocity. However, the details of this process and why it only affects velocity prediction are difficult to understand from our dataset and require further investigation, such as through laboratory experiments. This observation is not inconsistent with the Hertz theory.

Regarding the frequency content, according to the feature importance the full spectrum (FFT) of the whole signal carries less information than the spectrograms and the filtered waveforms. This is unexpected as according to the Hertz theory the full spectrum of the signal (maximum amplitude, variance, corner frequency) should all be highly dependent on the mass and the velocity of the impactor. This suggests that the temporal variation of the seismic signal spectrum (i.e. spectrograms) is more important in the prediction process and hence carry more information on the source properties than the information we can obtain from the full frequency spectrum itself.

We found that with the 114 selected features, our machine learning model more accurately predicts the velocity of the block at impact than its mass. According to a study by Kuehnert et al. (2020a) on real rockfalls at the Piton de la Fournaise Volcano, the maximum impact force and the resulting seismic signal amplitude are highly sensitive to variations in impact speed, while the frequency content of the seismic signal is most sensitive to the density and Young's modulus of the impactor and impacted plane. Given that all blocks and impacted zones had similar elastic properties in our study, it is likely that the variability of impacted forces and the resulting seismic signals were primarily influenced by changes in velocity rather than mass. This could help to explain why features based solely on the frequency spectrum of the seismic signals appeared to be less important in our regression analysis than those containing information on the amplitude of the seismic signals. Therefore, we think that in our case the seismic signals feature range is primarily influenced by changes in velocity rather than mass, making it easier for our machine learning model to predict velocity and potentially explaining some of our earlier findings.

5 Conclusions and perspectives

From the experimental single-block controlled launches conducted in the Riou-Bourdoux torrent, we demonstrated that a machine learning model based on the Random Forest algorithm is able to provide estimate of the mass and the velocity of the block at each impacts with an average error of around 25% for the mass and 10% for the velocity. With this new approach, we obtain a prediction accuracy on these two quantities equivalent to or better than all previous studies focusing on the high frequencies of the seismic signals generated by mass movements, which gave errors ranging from 20% to 400% of the target values (e.g., Hibert et al., 2011; Dammeier et al., 2011; Farin et al., 2015; Hibert et al., 2017b; Le Roy et al., 2019).

The machine learning model uses solely the features of the recorded signals and does not require an attenuation model to estimate the source properties conversely to the approaches based on the computation of the seismic energy and the maximum amplitude at the source. This removes the need to make assumptions which are necessary in the classical approaches used until now but which are carrying strong uncertainties, such as the velocity of the seismic waves, the density of the soil, the anelastic attenuation factor and the attenuation model used. The machine learning approach also removes the need to know the exact localisation of the impacts and to correct for site effects. Those are major advantages for an operational implementation of such methods for rockfall risks assessment and mitigation. An implementation in any context will only require to perform several, well-monitored, controlled launches of rockfalls to produce a dataset to train the machine learning model, which will then be able to predict the mass and the velocity of future rockfalls. Another strength of the Random Forest approach is its ability to perform well even with few events used to train the algorithm. Finally we use the same seismic signal features to predict the mass and the velocity of rockfalls that are already used to detect and identify seismic sources associated with mass wasting processes (Provost et al., 2017; Hibert et al., 2017c; Maggi et al., 2017; Wenner et al., 2021). This opens the prospect to build a detection system, based on seismic waves, that is able to tell when a rockfall occurs, what is its mass and velocity and possibly its localisation, all at the same time and even in near real-time given the possibility to easily record and broadcast seismic data.

It is further important to note that this experiment was performed in a controlled context, with an ideal setup, with simple mono-block rockfalls which travelled roughly along the same path, and with a seismic network very close to the sources. The machine learning based approach must now be experienced with more complex sources, such as multi-blocks rockfalls and even granular flows, and with more distant seismic stations. The station distances might hinder the ability of the machine learning model to estimate source properties, as the farthest we are from the source, the more we lose information due to propagation effects on seismic waves. However, the recent successes (Provost et al., 2017; Hibert et al., 2019; Wenner et al., 2021; Chmiel et al., 2021) in identifying mass wasting sources at medium to long distances, with the same approach and the same features, suggest that even when recording seismic signals far from the source, seismic signals retain information on the source properties in the higher frequency band (above 1 Hz), that could allow to determine those properties using the same approach. This would be a major breakthrough as it would allow to determine source properties for most landslides which do not generate seismic waves with enough energy in the lowest frequency bands to allow for an inversion of the properties of the source. This will be the subject of future work.

Finally, this approach based on machine learning algorithms might be applied to the analysis of other environmental processes for which classical seismological source inversion methods are not suitable. This could be used for the determination of properties (mass, velocity, flux, volume, forces, momentum, etc.) of sources that generate tremors (volcanic eruptions, debris flows, intense storms), complex high-frequency and even low-frequency signals (ice-calving events, hydro-acoustic signals) or even anthropogenic noises (vehicles, pumps). However, as for every machine learning based approach, sets of calibrated and well known examples are necessary to train the models. Physical models can also help by producing physically-based synthetic seismic signals. Regression of seismic source properties using machine learning approaches is a new complementary and interesting tool for the community interested in exotic or environmental seismic sources relevant for improving our understanding of these processes.

Code and data availability. All the pre-processed data, the raw seismic data and the code to compute the signal features are accessible at https://doi.org/10.5281/zenodo.6393210.

Author contributions. C.H., F.N., M.J., J.-.P.M. and F.B. conceptualized the research. C.H. processed the seismic data, implemented the machine learning approach and wrote the original draft. F.N., D.T. and F.B. processed the trajectory data. F.N., M.J., A.C., C.H., F.B and J.P.M. validated the trajectory reconstruction approach. All the authors participated and helped to conduct the controlled launch experiment. All the authors reviewed and edited the original draft. J.-.P.M. and M.J. funded this research.

Competing interests. The authors declare no competing interests

Acknowledgements. This work was carried with the support of the French National Research Agency (ANR) through the projects HYDROSLIDE "Hydrogeophysical Monitoring of Clayey Landslides", the Open Partial Agreement "Major Hazards" of Council of Europe through the project "Development of Cost-effective Ground-based and Remote Monitoring Systems for Detecting Landslide Initiation", the Research Council of Norway through its Centres of Excellence funding scheme, Project No. 262644. and the Observatoire Multi-disciplinaire des Instabilités de Versant (OMIV) (RESIF/OMIV, 2015). The authors thank H. Collomb (ONF-RTM / Alpes-de-Haute-Provence) for facilitating the access to the Riou-Bourdoux experimental site and Pierre Bottelin for insightful comments on the manuscript.

References

Aki, K. and Chouet, B.: Origin of coda waves: source, attenuation, and scattering effects, Journal of geophysical research, 80, 3322–3342, 1975.

Allstadt, K.: Extracting source characteristics and dynamics of the August 2010 Mount Meager landslide from broadband seismograms, Journal of Geophysical Research, 118, 1472–1490, https://doi.org/10.1002/jgrf.20110, 2013.

Allstadt, K., Matoza, R. S., Lockhart, A., Moran, S. C., Caplan-Auerbach, J., Haney, M., Thelen, W. A., and Malone, S. D.: Seismic and acoustic signatures of surficial mass movements at volcanoes, Journal of Volcanology and Geothermal Research, 2018.

Ao, Y., Li, H., Zhu, L., Ali, S., and Yang, Z.: Identifying channel sand-body from multiple seismic attributes with an improved random forest algorithm, Journal of Petroleum Science and Engineering, 173, 781–792, 2019.

Arran, M. I., Mangeney, A., de Rosny, J., Farin, M., Toussaint, R., and Roche, O.: Laboratory landquakes: Insights from experiments into the high-frequency seismic signal generated by geophysical granular flows, Earth and Space Science Open Archive ESSOAr, 2020.

Bachelet, V., Mangeney, A., De Rosny, J., Toussaint, R., and Farin, M.: Elastic wave generated by granular impact on rough and erodible surfaces, Journal of Applied Physics, 123, 044 901, 2018.

Bottelin, P., Jongmans, D., Daudon, D., Mathy, A., Helmstetter, A., Bonilla-Sierra, V., Cadet, H., Amitrano, D., Richefeu, V., Lorier, L., et al.: Seismic and mechanical studies of the artificially triggered rockfall at Mount Néron (French Alps, December 2011), Natural Hazards and Earth System Sciences, 14, 3175–3193, 2014.

Breiman, L.: Random forests, Machine learning, 45, 5–32, 2001.

Chao, W.-A., Wu, T.-R., Ma, K.-F., Kuo, Y.-T., Wu, Y.-M., Zhao, L., Chung, M.-J., Wu, H., and Tsai, Y.-L.: The large Greenland landslide of 2017: Was a tsunami warning possible?, Seismological Research Letters, 89, 1335–1344, 2018.

Chmiel, M., Walter, F., Wenner, M., Zhang, Z., McArdell, B. W., and Hibert, C.: Machine Learning improves debris flow warning, Geophysical Research Letters, p. e2020GL090874, 2021.

Crampin, S.: Higher modes of seismic surface waves: Second Rayleigh mode energy, Journal of Geophysical Research, 70, 5135–5143, 1965.

Dammeier, F., Moore, J. R., Haslinger, F., and Loew, S.: Characterization of alpine rockslides using statistical analysis of seismic signals, Journal of Geophysical Research, 116, F04 024, https://doi.org/10.1029/2011JF002037, 2011.

Dammeier, F., Moore, J. R., Hammer, C., Haslinger, F., and Loew, S.: Automatic detection of alpine rockslides in continuous seismic data using Hidden Markov Models, Journal of Geophysical Research: Earth Surface, 121, 351–371, 2016.

Deparis, J., Jongmans, D., Cotton, F., Baillet, L., Thouvenot, F., and Hantz, D.: Analysis of rock-fall and rock-fall avalanche seismograms in the French Alps, Bulletin of the Seismological Society of America, 98, 1781–1796, https://doi.org/10.1785/0120070082, 2008.

Dietze, M., Turowski, J. M., Cook, K. L., and Hovius, N.: Spatiotemporal patterns, triggers and anatomies of seismically detected rockfalls, Earth Surface Dynamics, 5, 757–779, 2017.

Dufresne, A., Wolken, G., Hibert, C., Bessette-Kirton, E., Coe, J. A., Geertsema, M., and Ekström, G.: The 2016 Lamplugh rock avalanche, Alaska: deposit structures and emplacement dynamics, Landslides, 16, 2301–2319, 2019.

Ekström, G. and Stark, C. P.: Simple scaling of catastrophic landslide dynamics, Science, 339, 1416–1419, https://doi.org/10.1126/science.1232887, 2013.

Farin, M., Mangeney, A., Toussaint, R., Rosny, J. d., Shapiro, N., Dewez, T., Hibert, C., Mathon, C., Sedan, O., and Berger, F.: Characterization of rockfalls from seismic signal: Insights from laboratory experiments, Journal of Geophysical Research: Solid Earth, 120, 7102–7137, https://doi.org/10.1002/2015JB012331, 2015JB012331, 2015.

Farin, M., Mangeney, A., De Rosny, J., Toussaint, R., Sainte-Marie, J., and Shapiro, N. M.: Experimental validation of theoretical methods to estimate the energy radiated by elastic waves during an impact, Journal of Sound and Vibration, 362, 176–202, 2016.

Farin, M., Mangeney, A., De Rosny, J., Toussaint, R., and Trinh, P.-T.: Relations between the characteristics of granular column collapses and resultant high-frequency seismic signals, Journal of Geophysical Research: Earth Surface, 124, 2987–3021, 2019.

Gance, J., Grandjean, G., Samyn, K., and Malet, J.-P.: Quasi-Newton inversion of seismic first arrivals using source finite bandwidth assumption: Application to subsurface characterization of landslides, Journal of Applied Geophysics, 87, 94–106, 2012.

Gracchi, T., Lotti, A., Saccorotti, G., Lombardi, L., Nocentini, M., Mugnai, F., Gigli, G., Barla, M., Giorgetti, A., Antolini, F., et al.: A method for locating rockfall impacts using signals recorded by a microseismic network, Geoenvironmental Disasters, 4, 1–12, 2017.

Hertz, H.: Über die Berührung fester elastischer Körper., Journal für die reine und angewandte Mathematik, 92, 156–171, 1882.

Hibert, C., Mangeney, A., Grandjean, G., and Shapiro, N. M.: Slope instabilities in Dolomieu crater, Réunion Island: From seismic signals to rockfall characteristics, Journal of Geophysical Research, 116, F04 032, https://doi.org/10.1029/2011JF002038, 2011.

Hibert, C., Grandjean, G., Bitri, A., Travelletti, J., and Malet, J.-P.: Characterizing landslides through geophysical data fusion: Example of the La Valette landslide (France), Engineering Geology, 128, 23–29, 2012.

Hibert, C., Mangeney, A., Grandjean, G., Baillard, C., Rivet, D., Shapiro, N. M., Satriano, C., Maggi, A., Boissier, P., Ferrazzini, V., et al.: Automated identification, location, and volume estimation of rockfalls at Piton de la Fournaise volcano, Journal of Geophysical Research: Earth Surface, 119, 1082–1105, 2014a.

Hibert, C., Stark, C. P., and Ekström, G.: Seismology of the Oso-Steelhead landslide, Nat. Hazards Earth Syst. Sci. Discuss., pp. 7309–7327, 2014b.

Hibert, C., Ekström, G., and Stark, C. P.: The relationship between bulk-mass momentum and short-period seismic radiation in catastrophic landslides, Submited to Journal of Geophysical Research: Earth Surface, 2017a.

Hibert, C., et al., Malet, J.-P., Bourrier, F., Provost, F., Berger, F., Bornemann, P., Tardif, P., and Mermin, E.: Single-block rockfall dynamics inferred from seismic signal analysis, Earth Surface Dynamics, 5, 283–292, 2017b.

Hibert, C., Provost, F., Malet, J.-P., Maggi, A., Stumpf, A., and Ferrazzini, V.: Automatic identification of rockfalls and volcano-tectonic earthquakes at the Piton de la Fournaise volcano using a Random Forest algorithm, Journal of Volcanology and Geothermal Research, 340, 130–142, 2017c.

Hibert, C., Michéa, D., Provost, F., Malet, J., and Geertsema, M.: Exploration of continuous seismic recordings with a machine learning approach to document 20 yr of landslide activity in Alaska, Geophysical Journal International, 219, 1138–1147, 2019.

Huang, C.-J., Yin, H.-Y., Chen, C.-Y., Yeh, C.-H., and Wang, C.-L.: Ground vibrations produced by rock motions and debris flows, Journal of Geophysical Research: Earth Surface, 112, 2007.

Iverson, R., George, D., Allstadt, K., Reid, M., Collins, B., Vallance, J., Schilling, S., Godt, J., Cannon, C., Magirl, C., et al.: Landslide mobility and hazards: implications of the 2014 Oso disaster, Earth and Planetary Science Letters, 412, 197–208, 2015.

Kanamori, H. and Given, J. W.: Analysis of long-period seismic waves excited by the May 18, 1980, eruption of Mount St. Helens - A terrestrial monopole?, Journal of Geophysical Research, 87, 5422–5432, https://doi.org/10.1029/JB087iB07p05422, 1982.

Kanamori, H., Given, J. W., and Lay, T.: Analysis of seismic body waves excited by the Mount St. Helens eruption of May 18, 1980, Journal of Geophysical Research, 89, 1856–1866, 1984.

Kawakatsu, H.: Centroid single force inversion of seismic waves generated by landslides, Journal of Geophysical Research: Solid Earth, 94, 12 363–12 374, 1989.

Kuehnert, J., Mangeney, A., Capdeville, Y., Métaxian, J.-P., Bonilla, L., Stutzmann, E., Chaljub, E., Boissier, P., Brunet, C., Kowalski, P., et al.: Simulation of Topography Effects on Rockfall-Generated Seismic Signals: Application to Piton de la Fournaise Volcano, Journal of Geophysical Research: Solid Earth, 125, 2020a.

Kuehnert, J., Mangeney, A., Capdeville, Y., Vilotte, J.-P., Stutzmann, E., Chaljub, E., El-Madani, A., BOISSIER, P., Brunet, C., KOWALSKI, P., et al.: Rockfall localization based on inter-station ratios of seismic energy, Earth and Space Science Open Archive ESSOAr, 2020b.

Le Roy, G., Helmstetter, A., Amitrano, D., Guyoton, F., and Le Roux-mallouf, R.: Seismic analysis of the detachment and impact phases of a rockfall and application for estimating rockfall volume and free-fall height, Journal of Geophysical Research: Earth Surface, 124, 2602–2622, 2019.

Levy, C., Mangeney, A., Bonilla, F., Hibert, C., Calder, E. S., and Smith, P. J.: Friction weakening in granular flows deduced from seismic records at the Soufrière Hills Volcano, Montserrat, Journal of Geophysical Research: Solid Earth, 120, 7536–7557, 2015.

Li, Z., Huang, X., Xu, Q., Yu, D., Fan, J., and Qiao, X.: Dynamics of the Wulong landslide revealed by broadband seismic records, Earth, Planets and Space, 69, 1–10, 2017.

Loew, S., Hantz, D., and Gerber, W.: Rockfall Causes and Transport Mechanisms-A Review, Reference Module in Earth Systems and Environmental Sciences, 2021.

Maggi, A., Ferrazzini, V., Hibert, C., Beauducel, F., Boissier, P., and Amemoutou, A.: Implementation of a multistation approach for automated event classification at Piton de la Fournaise volcano, Seismological Research Letters, 88, 878–891, 2017.

Malfante, M., Dalla Mura, M., Mars, J. I., Métaxian, J.-P., Macedo, O., and Inza, A.: Automatic classification of volcano seismic signatures, Journal of Geophysical Research: Solid Earth, 2018.

Maquaire, O., Malet, J.-P., Remaıtre, A., Locat, J., Klotz, S., and Guillon, J.: Instability conditions of marly hillslopes: towards landsliding or gullying? The case of the Barcelonnette Basin, South East France, Engineering Geology, 70, 109–130, 2003.

Moore, J. R., Pankow, K. L., Ford, S. R., Koper, K. D., Hale, J. M., Aaron, J., and Larsen, C. F.: Dynamics of the Bingham Canyon rock avalanches (Utah, USA) resolved from topographic, seismic, and infrasound data, Journal of Geophysical Research: Earth Surface, 122, 615–640, 2017.

Moretti, L., Mangeney, A., Walter, F., Capdeville, Y., Bodin, T., Stutzmann, E., and Le Friant, A.: Constraining landslide characteristics with Bayesian inversion of field and seismic data, Geophysical Journal International, 221, 1341–1348, 2020.

Noël, F., Wyser, E., Jaboyedoff, M., Derron, M.-H., Cloutier, C., Turmel, D., and Locat, J.: Real-size rockfall experiment: How different rockfall simulation impact models perform when confronted with reality?, Geohazards 7 Engineering Resiliency in a Changing Climate, 2017.

Noël, F., Jaboyedoff, M., Caviezel, A., Hibert, C., Bourrier, F., and Malet, J.-P.: Rockfall trajectory reconstruction: A flexible method utilizing video footage and high-resolution terrain models, Earth Surface Dynamics Discussions, 2022, 1–30, https://doi.org/10.5194/esurf-2022-16, 2022.

Norris, R. D.: Seismicity of rockfalls and avalanches at three Cascade Range volcanoes: Implications for seismic detection of hazardous mass movements, Bulletin of the Seismological Society of America, 84, 1925–1939, 1994.

Pérez, N., Venegas, P., Benitez, D., Grijalva, F., Lara, R., and Ruiz, M.: Benchmarking Seismic-Based Feature Groups to Classify the Cotopaxi Volcanic Activity [-4pt], IEEE Geoscience and Remote Sensing Letters, 2020.

Provost, F., Hibert, C., and Malet, J.-P.: Automatic classification of endogenous landslide seismicity using the Random Forest supervised classifier, Geophysical Research Letters, 44, 113–120, 2017.

Rouet-Leduc, B., Hulbert, C., Lubbers, N., Barros, K., Humphreys, C. J., and Johnson, P. A.: Machine learning predicts laboratory earthquakes, Geophysical Research Letters, 44, 9276–9282, 2017.

Saló, L., Corominas, J., Lantada, N., Matas, G., Prades, A., and Ruiz-Carulla, R.: Seismic energy analysis as generated by impact and fragmentation of single-block experimental rockfalls, Journal of Geophysical Research: Earth Surface, 123, 1450–1478, 2018.

Schneider, D., Huggel, C., Haeberli, W., and Kaitna, R.: Unraveling driving factors for large rock–ice avalanche mobility, Earth Surface Processes and Landforms, 36, 1948–1966, 2011.

Vilajosana, I., Suriñach, E., Abellán, A., Khazaradze, G., Garcia, D., and Llosa, J.: Rockfall induced seismic signals: case study in Montserrat, Catalonia, Natural Hazards and Earth System Sciences, 8, 805–812, https://doi.org/10.5194/nhess-8-805-2008, 2008.

Volkwein, A., Schellenberg, K., Labiouse, V., Agliardi, F., Berger, F., Bourrier, F., Dorren, L. K., Gerber, W., and Jaboyedoff, M.: Rockfall characterisation and structural protection–a review, Natural Hazards and Earth System Sciences, 11, 2617–2651, 2011.

Wenner, M., Hibert, C., van Herwijnen, A., Meier, L., and Walter, F.: Near-real-time automated classification of seismic signals of slope failures with continuous random forests, Natural Hazards and Earth System Sciences, 21, 339–361, 2021.

Wyllie, D. C.: Rock fall engineering: development and calibration of an improved model for analysis of rock fall hazards on highways and railways, Ph.D. thesis, University of British Columbia, 2014.

Yamada, M., Matsushi, Y., Chigira, M., and Mori, J.: Seismic recordings of landslides caused by Typhoon Talas (2011), Japan, Geophysical Research Letters, 39, L13 301, https://doi.org/10.1029/2012GL052174, 2012.

Yan, Y., Li, T., Liu, J., Wang, W., and Su, Q.: Monitoring and early warning method for a rockfall along railways based on vibration signal characteristics, Scientific reports, 9, 1–10, 2019.

Zhang, Z., He, S., Liu, W., Liang, H., Yan, S., Deng, Y., Bai, X., and Chen, Z.: Source characteristics and dynamics of the October 2018 Baige landslide revealed by broadband seismograms, Landslides, 16, 777–785, 2019.

Zhao, J., Moretti, L., Mangeney, A., Stutzmann, E., Kanamori, H., Capdeville, Y., Calder, E. S., Hibert, C., Smith, P. J., Cole, P., et al.: Model Space Exploration for Determining Landslide Source History from Long-Period Seismic Data, Pure and Applied Geophysics, pp. 1–25, 2012.

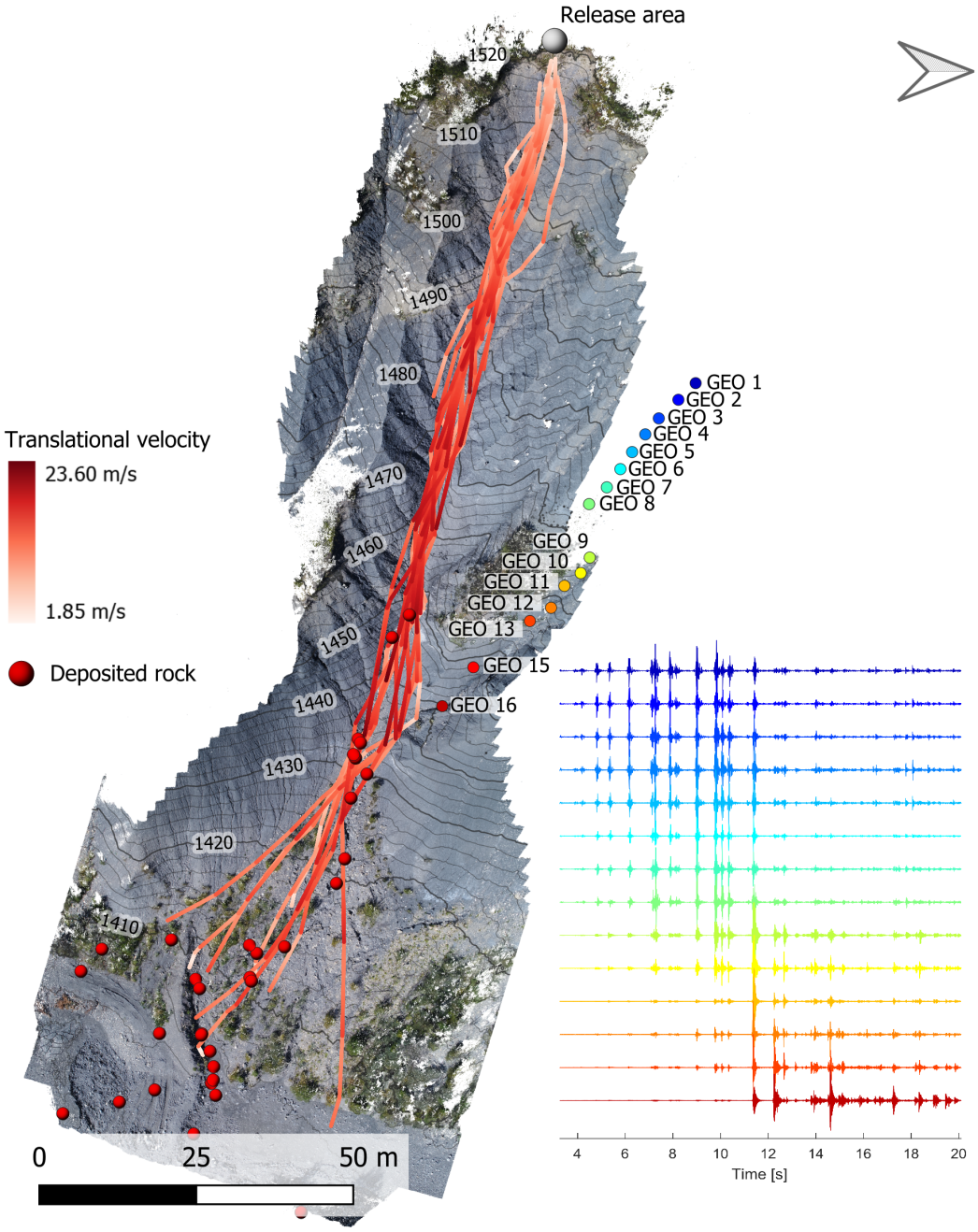

Figure 1. Orthophotography of the Riou-Bourdoux gully, with the reconstructed trajectory of all the blocks, and the location of the geophones used in this study indicated by colored dots. The color of the trajectory scale with the absolute translational velocity of the block. The raw seismic signals recorded at each geophone for the first launch are represented on the right, in the color corresponding to the one of the dots indicating the location of the sensor.

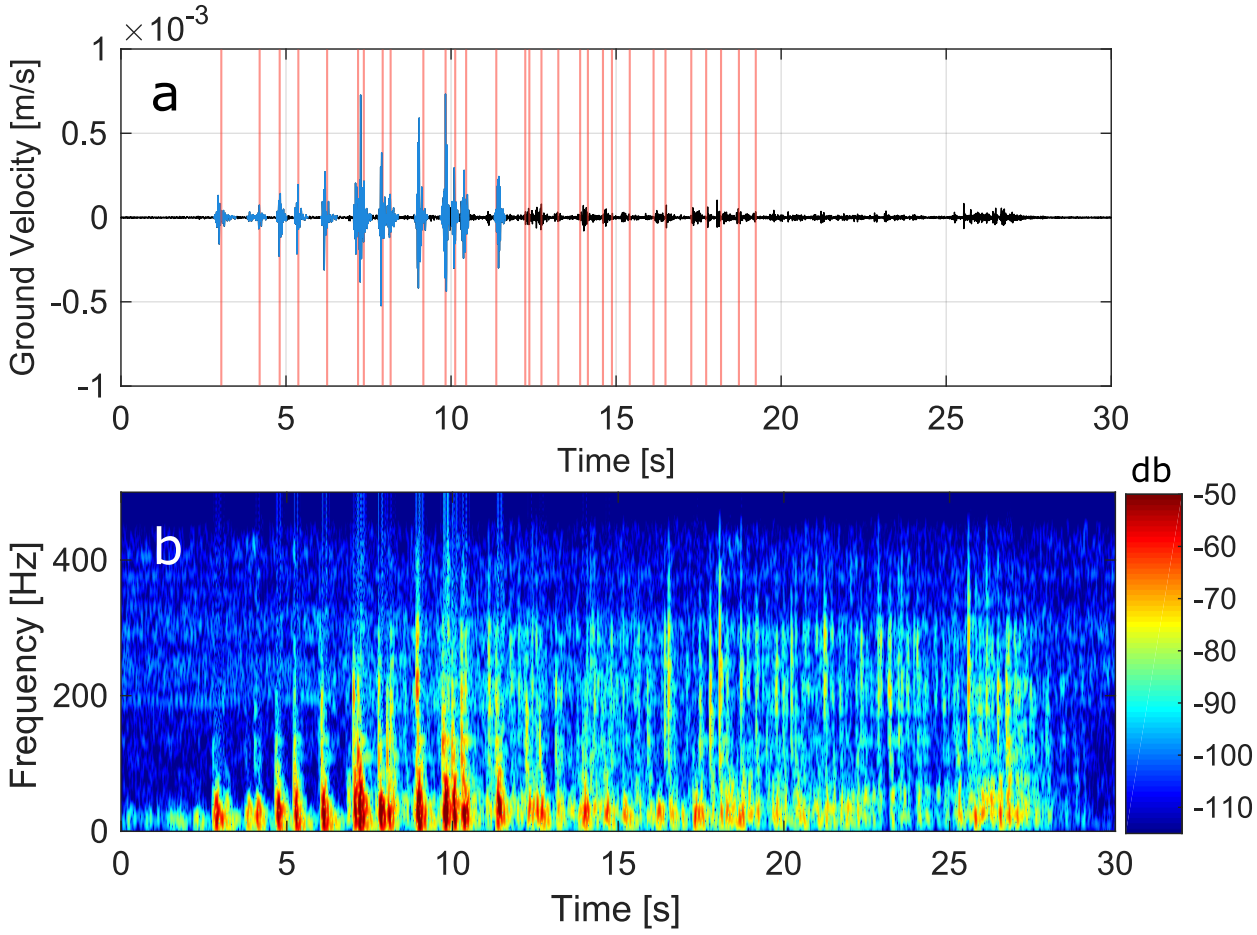

Figure 2. Seismic signal (a) and spectrogram (b) generated by impacts of the Block #1 and recorded on geophone 1. The selected seismic signals used in our analysis are indicated in blue. The impact times derived from the camera-based workflow for this launch are indicated by red lines on pannel (a).

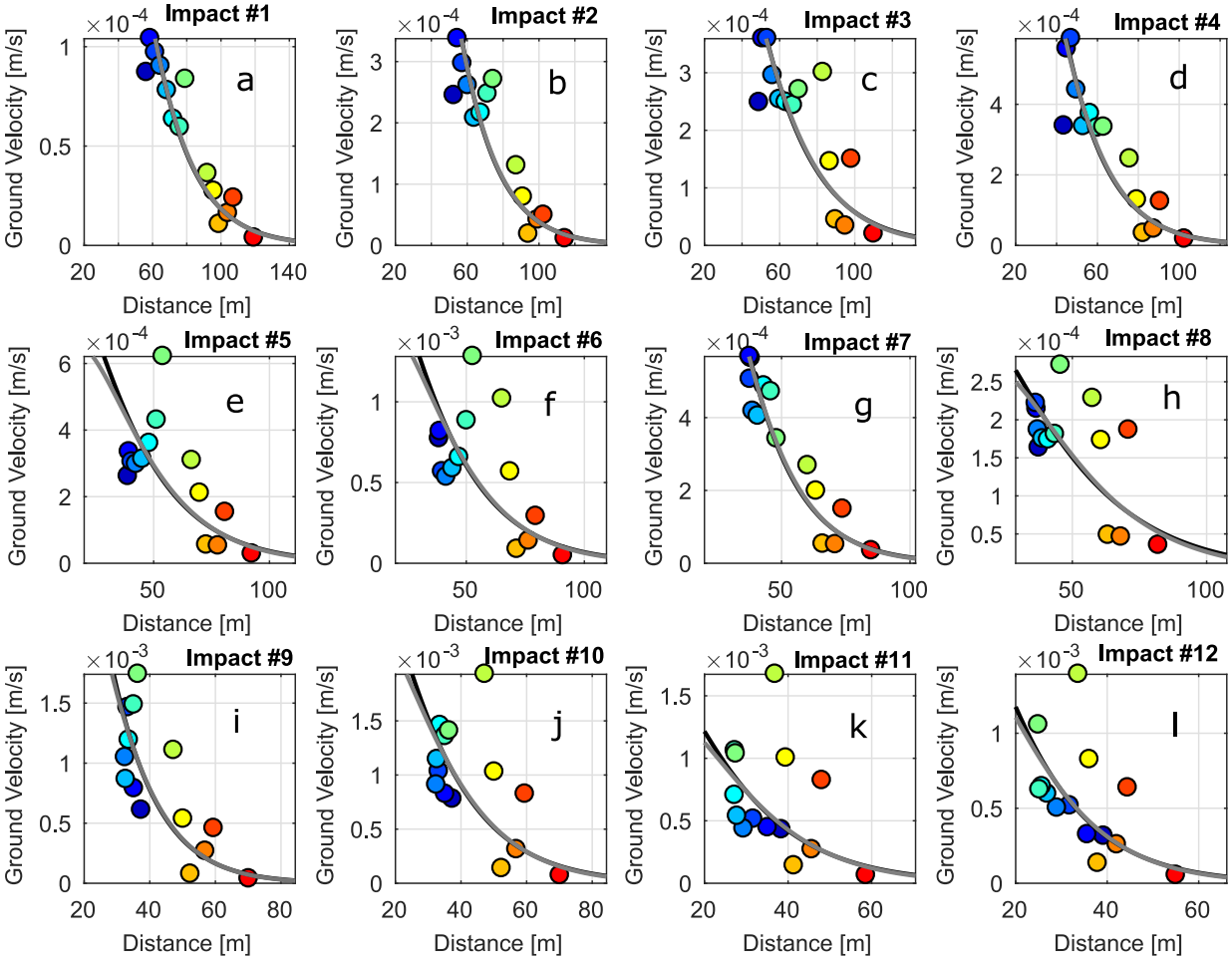

Figure 3. Maximum envelope amplitude as a function of the distance for each impact and each geophone for the block #1. The colour corresponds to the colour of the geophones on Figure 1. The black line indicates the best regression computed with the model assuming a signal dominated by surface waves (1) and the dark gray one assuming a signal dominated by body waves (2).

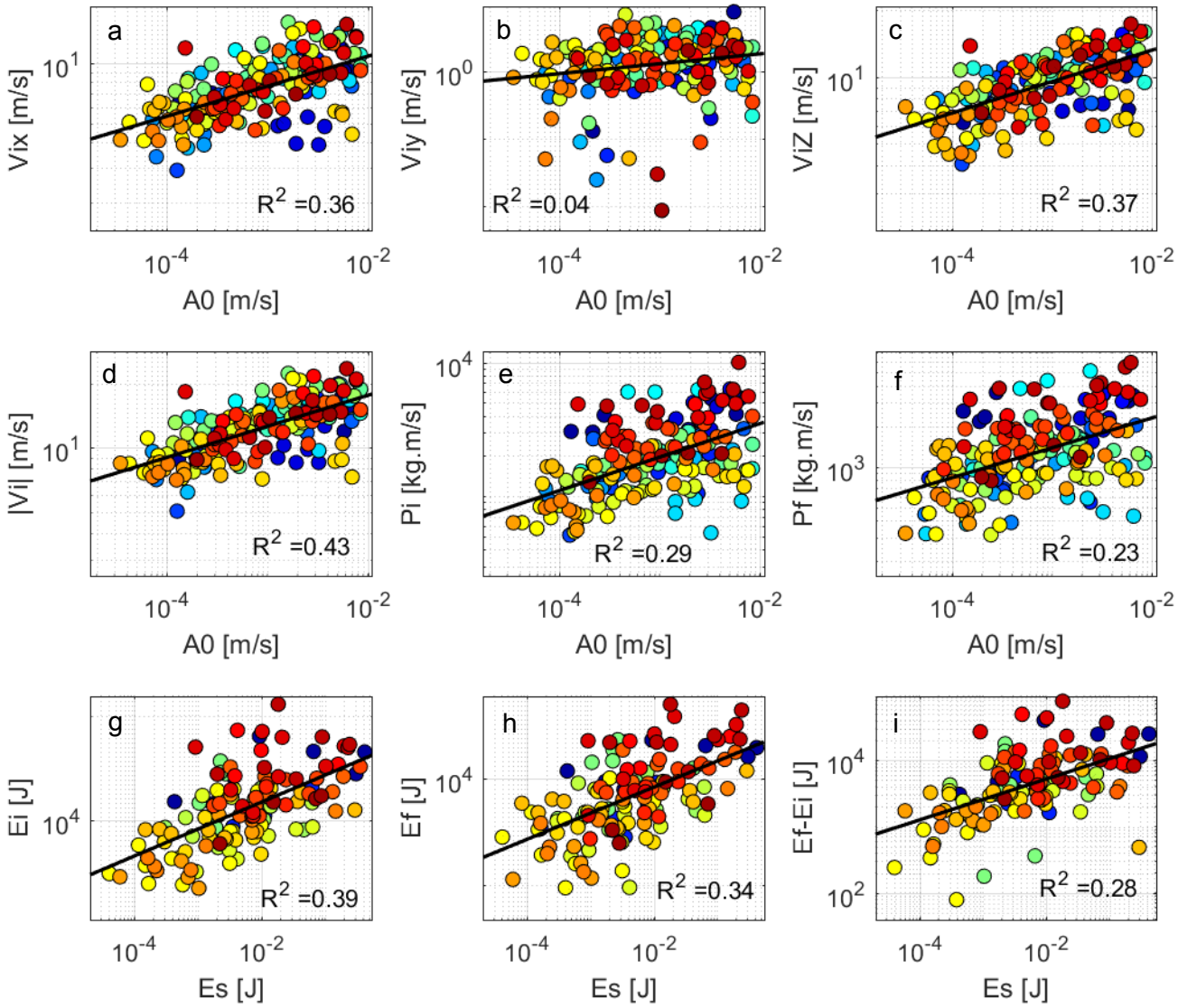

Figure 4. Correlation between the seismic and trajectography properties of the blocks: a) the eastbound incident velocity, b) the northbound incident velocity, c) the vertical incident velocity, d) the modulus of the incident velocity and e) the incident total momentum and f) the restituted momentum as a function of the maximum amplitude at the source A_0; g) the incident kinetic energy, h) the restituted kinetic energy and i) the difference of both as a function of the seismic energy E_s. The black line indicates the best linear regression, with the coefficient of determination R^2 indicated in the panel. Dots of the same color are from the same rockfall launch (i.e. identical block mass).

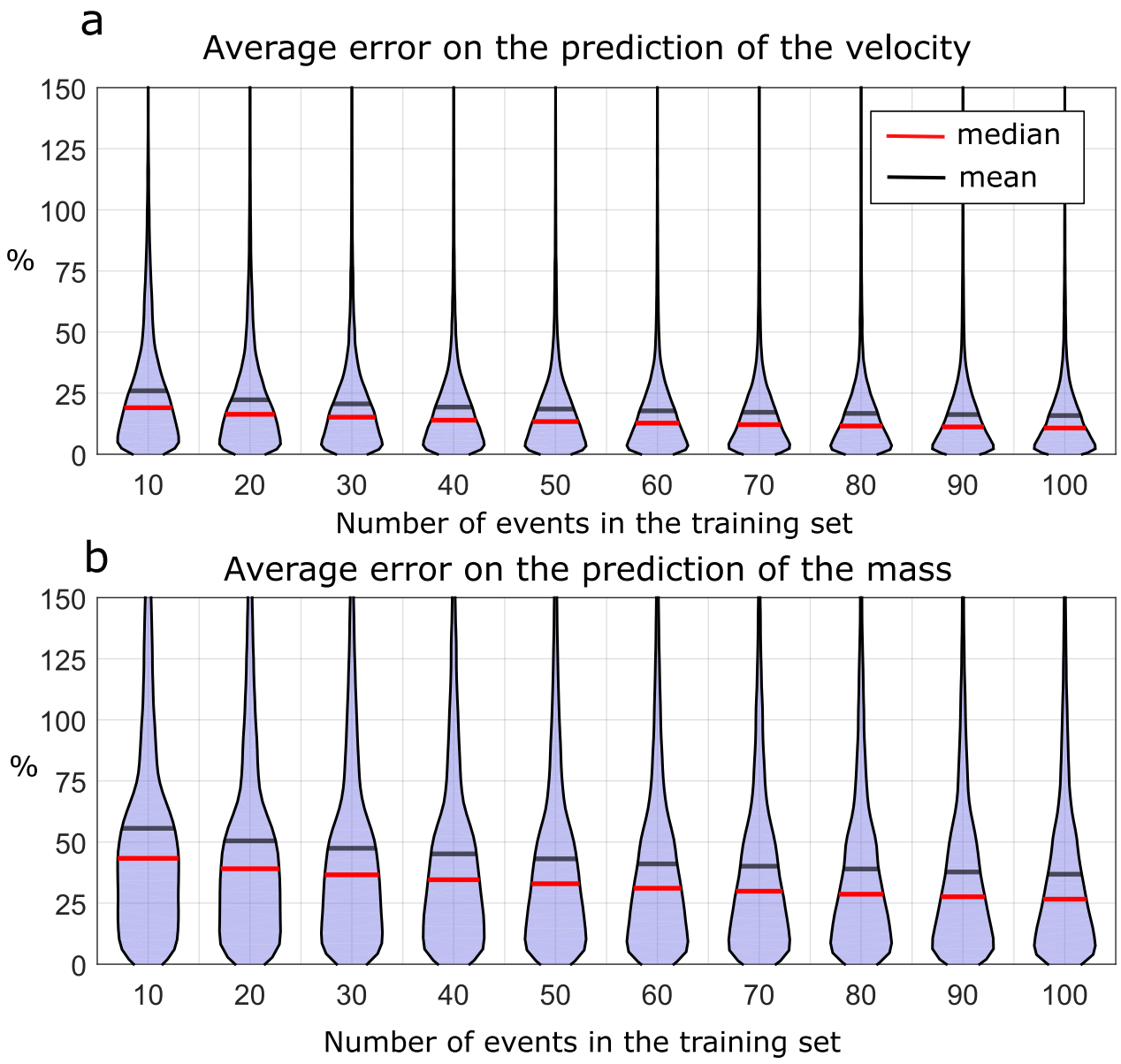

Figure 5. Distribution of the error (%) over 100 instance of training and testing the Random Forest model for the prediction of the mass values when trained with 10 to 100 samples to predict a) the velocity and b) the mass. The mean error is indicated by a black line, the median by a red line.

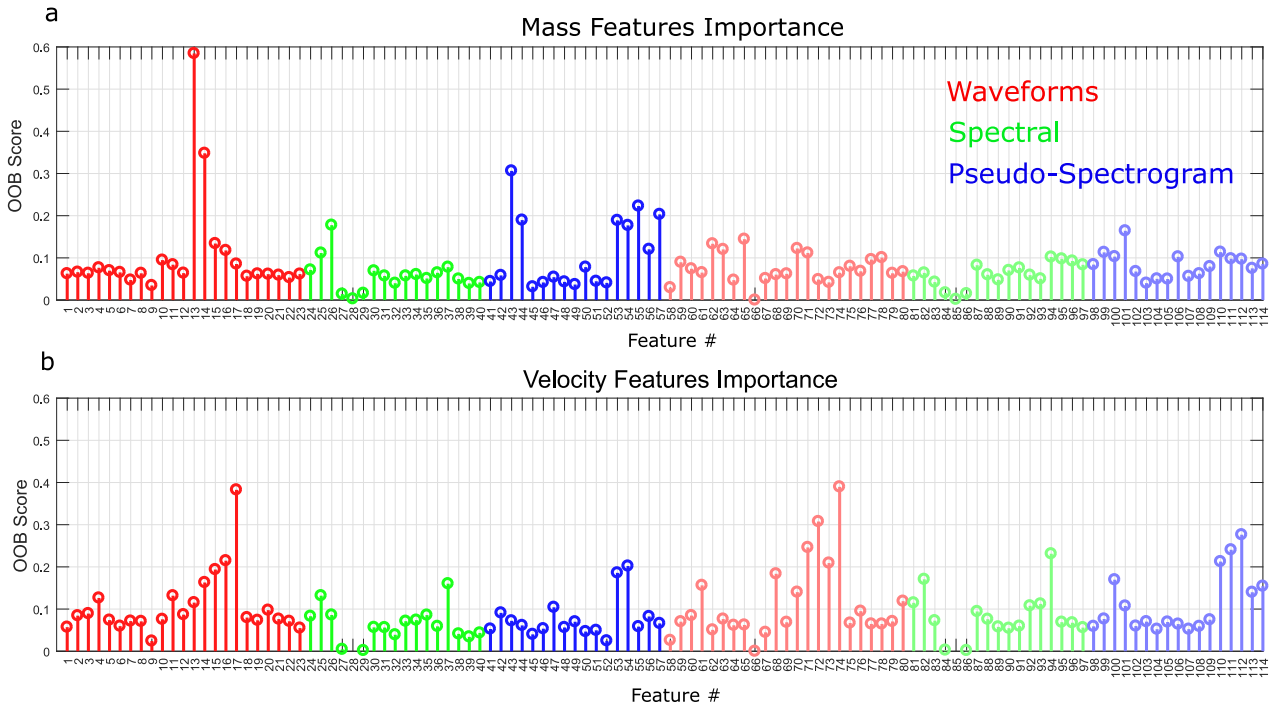

Figure 6. Importance score of the features for the prediction of a) the mass and b) the velocity. Colors indicate the family of features (waveform, spectral or pseudo-spectrogram). Bright color correspond to the mean of the feature while dimmed colors correspond to the standard deviation of the features. The description of each feature and their respective numbers can be found in Appendix A.

Table A1. Features table

Number	Name	Formula
	Waveform attributes:	
1 (58)	Duration	$T = t_e - t_s$
2 (59)	RappMaxMean	$\max[e(t)]/\mathrm{mean}[e(t)]$
3 (60)	RappMaxMedian	$\max[e(t)]/\mathrm{median}[e(t)]$
4 (61)	AsDec	$(t_{\max} - t_s)/(t_e - t_{\max})$
5 (62)	KurtoSig	$\mathrm{Kurt[s(t)]}$
6 (63)	KurtoEnv	$\mathrm{Kurt[e(t)]}$
7 (64)	SkewSig	$\mathrm{Skew[s(t)]}$
8 (65)	SkewEnv	$\mathrm{Skew[e(t)]}$
9 (66)	CorPeakNumber	number of peaks in $a(\tau)$
10 (67)	Energy1/3Cor	$\int_0^{\mathrm{T}/3} \mathrm{a}(\tau)\mathrm{d}\tau$
11 (68)	Energy2/3Cor	$\int_{\mathrm{T}/3}^{\mathrm{T}} \mathrm{a}(\tau)\mathrm{d}\tau$
12 (69)	int_ratio	$\int_0^{\mathrm{T}/3} \mathrm{a}(\tau)\mathrm{d}\tau / \int_{\mathrm{T}/3}^{\mathrm{T}} \mathrm{a}(\tau)\mathrm{d}\tau$
13-17 (70-74)	ES1 to ES5	$\mathrm{ES}_i = \log_{10} \int e_i(t)dt$
18-22 (75-79)	KurtoF1 to KurtoF5	$\frac{\mathrm{Kurt}[s_i(t)]}{\sqrt{e(t) - l(t)^2}}$
23 (80)	RMSDecPhaseLine	
	Spectral attributes:	
24 (81)	MeanFFT	$\mathrm{mean}[\lvert S(\nu)\rvert]$
25 (82)	MaxFFT	$\max[\lvert S(\nu)\rvert]$
26 (83)	FMaxFFT	$\nu_{\max}$
27 (84)	MedianFFT	$\mathrm{median}[\lvert S(\nu)\rvert]$
28 (85)	VarFFT	$\mathrm{var}[\lvert S(\nu)\rvert]$
29 (86)	FCentroid	$\mathrm{centroid}\,[\lvert S(\nu)\rvert]$
30 (87)	Fquart1	$\mathrm{centroid}\,[\lvert S(\nu)\rvert_1]$
31 (88)	Fquart3	$\mathrm{centroid}\,[\lvert S(\nu)\rvert_3]$
32 (89)	NPeakFFT	number of peaks in $\lvert S(\nu)\rvert > 0.75\lvert S(\nu)\rvert_{\max}$
33 (90)	MeanPeaksFFT	$\mathrm{mean}\,[\lvert S(\nu)\rvert \mathrm{at\ peaks}]$
34-37 (91-94)	E1FFT to E4FFT	$\mathrm{E}_i\mathrm{FFT} = \int \lvert S(\nu)\rvert_i d\nu$
38 (95)	gamma1	$\gamma_1 = \sum \nu \lvert S(\nu)\rvert^2 / \sum \lvert S(\nu)\rvert^2$
39 (96)	gamma2	$\gamma_2 = \sqrt{\sum \nu^2 \lvert S(\nu)\rvert^2 / \sum \lvert S(\nu)\rvert^2}$
40 (97)	gammas	$\sqrt{\lvert\gamma_1^2 - \gamma_2^2\rvert}$
	Pseudo-spectrogram attributes:	
41 (98)	KurtoMaxDFT	$\mathrm{Kurt}[\max[\lvert \mathrm{DFT(t,\omega)}\rvert]]$
42 (99)	KurtoMedianDFT	$\mathrm{Kurt}[\mathrm{median}[\lvert \mathrm{DFT(t,\omega)}\rvert]]$
43 (100)	MaxOverMeanDFT	$\mathrm{mean}[\frac{\max[\lvert \mathrm{DFT(t,\omega)}\rvert]}{\mathrm{mean}[\lvert \mathrm{DFT(t,\omega)}\rvert]}]$
44 (101)	MaxOverMedianDFT	$\mathrm{mean}[\frac{\max[\lvert \mathrm{DFT(t,\omega)}\rvert]}{\mathrm{median}[\lvert \mathrm{DFT(t,\omega)}\rvert]}]$
45 (102)	NbrPeaksMaxDFT	Number of peaks in $\max[\lvert \mathrm{DFT(t,\omega)}\rvert]$
46 (103)	NbrPeaksMeanDFT	Number of peaks in $\mathrm{mean}[\lvert \mathrm{DFT(t,\omega)}\rvert]$
47 (104)	NbrPeaksMedianDFT	Number of peaks in $\mathrm{median}[\lvert \mathrm{DFT(t,\omega)}\rvert]$
48 (105)	Ratio between 45 and 46	–
49 (106)	Ratio between 45 and 47	–
50 (107)	NbrPeaksCentralFreq	Number of peaks in $\mathrm{median}[\lvert \mathrm{DFT(t,\omega_2)}\rvert]$
51 (108)	NbrPeaksMaxFreq	Number of peaks in $\mathrm{median}[\lvert \mathrm{DFT(t,\omega_{max})}\rvert]$
52 (109)	Ratio between 50 and 51	–
53 (110)	DistMaxMeanFreqDTF	$\mathrm{mean}[\max[\lvert \mathrm{DFT(t,\omega)}\rvert] - \mathrm{mean}[\lvert \mathrm{DFT(t,\omega)}\rvert]]$
54 (111)	DistMaxMedianFreqDTF	$\mathrm{mean}[\max[\lvert \mathrm{DFT(t,\omega)}\rvert] - \mathrm{median}[\lvert \mathrm{DFT(t,\omega)}\rvert]]$
55 (112)	DistQ2Q1DFT	$\mathrm{mean}[\mathrm{centroid}[\lvert \mathrm{DFT(t,\omega)}\rvert_2] - \mathrm{centroid}[\lvert \mathrm{DFT(t,\omega)}\rvert_1]]$
56 (113)	DistQ3Q2DFT	$\mathrm{mean}[\mathrm{centroid}[\lvert \mathrm{DFT(t,\omega)}\rvert_3] - \mathrm{centroid}[\lvert \mathrm{DFT(t,\omega)}\rvert_2]]$
57 (114)	DistQ3Q1DFT	$\mathrm{mean}[\mathrm{centroid}[\lvert \mathrm{DFT(t,\omega)}\rvert_3] - \mathrm{centroid}[\lvert \mathrm{DFT(t,\omega)}\rvert_1]]$

Number for standard deviation of feature is given in parentheses. Waveform- and spectrum-based features, with $s(t)$ the windowed raw seismogram, $e(t)$ its envelope, $l(t) = e_{max} - \frac{e_{max}}{t_f - t_{max}} t$, $a(\tau)$ its auto-correlation function, $s_i(t)$ the windowed seismograms filtered in the 5–10 Hz ($i = 1$), 10–30 Hz ($i = 2$), 30–50 Hz ($i = 3$), 50–100 Hz ($i = 4$), 100–199 Hz ($i = 5$) frequency bands, $e_i(t)$ their corresponding envelopes, t_s and t_e the start and end times of the window, $t_{\max}$ the time of the maximum amplitude, $\mathrm{Kurt}(X) = \frac{\mu_4(X)}{\sigma^4(X)}$ the Kurtosis of distribution X where $\mu_4(X)$ indicates the fourth moment of X and σ its standard deviation, $\mathrm{Skew}(X) = \frac{\mu_3(X)}{\sigma^3(X)}$ the Skewness of distribution X where μ_3 indicates the third moment of X, $S(\nu)$ the fast Fourier transform of $s(t)$, $\nu_{\max}$ the frequency at which $|S(\nu)|$ is maximum, $|S(\nu)|_i$ the ith quartile of $|S(\nu)|$, $DFT(t,\omega)$ is the discrete Fourier transform of $s(t)$, ω_2 the central frequency of $DFT(t,\omega)$, $\omega_{\max}$ the frequency at the maximum of $DFT(t,\omega)$, $|DFT(t,\omega)|_j$ the jth quartile of $|DFT(t,\omega)|$.